Eur. Phys. J. D (2020) 74: 12
https://doi.org/10.1140/epjd/e2019-100541-5

THE EUROPEAN PHYSICAL JOURNAL D

Regular Article

The Auger spectra in argon induced by electron impact – new measurements with high resolution*

Jozo J. Jureta[1], Bratislav P. Marinković[1,a], and Lorenzo Avaldi[2]

[1] Institute of Physics Belgrade, University of Belgrade, Laboratory for Atomic Collision Processes, Pregrevica 118, 11080 Belgrade, Serbia
[2] CNR-Istituto di Struttura della Materia, Area della Ricerca di Roma 1, CP10, 00015 Monterotondo, Scalo, Italy

Received 29 October 2019 / Received in final form 4 December 2019
Published online 24 January 2020

Abstract. The Auger spectrum of argon in the kinetic energy region (135–235 eV) has been measured using a non-monochromatic electron beam (incident energy from 313 to 2019 eV) at two ejection angles of 60° and 90° with a high resolution electrostatic analyzer. The electron impact energies of 313 and 323 eV have been used in order to disentangle the contribution of the ionization and decay of the $2s$ state. The systematic analysis of the measured spectra shows the dominance of the Coster-Kronig transitions from the $2s$ ionization in the energy region 135–159 eV and 208–235 eV, while the Auger transitions from the $2p$ ionization are dominant in the energy region 160–208 eV. The high resolution of the present work led to the observation of a certain number of new features in two energy regions 135–159 and 208–235 eV, respectively. Recent literature data on the cascade Auger processes and threshold formation of Ar^{2+} satellite states allow the assignment of some of them, while other have been left without assignments. The influence of the PCI effect on the line-shape, width and energy position of the features in the kinetic energy region 200–208 eV has been also investigated and the PCI shift versus excess energy above threshold compared with previous data and theoretical predictions.

1 Introduction

Auger spectroscopy has been extensively used in the characterization of atoms/molecules and the environment they are embedded in, because the energies of the Auger transitions strongly depend on the structure of inner electronic orbitals and on the correlation among electrons in the emitting system. Indeed, Auger lines are a consequence of the non-radiative decay of a core hole and the re-arrangements of electrons within the atom and hence give an insight into the fast and ultrafast atomic phenomena. Despite a lot of attention being paid to the study of Auger spectra, even Auger spectra of rare gas atoms contain information not yet completely understood. In this paper we want to exploit the high sensitivity of our experimental set-up [1] to extend the region of observation of the ejected electrons in Ar due to the Auger processes beyond the one previously considered in electron impact measurements.

The L-MM Auger spectra in argon have been previously studied by X-rays [2], ions [3,4] and electron impacts [5–8]. Also the resonant Auger transitions, occurring when a $2p$ electron is promoted to an empty state, have been reported in [5,9], while the correlation effects have been thoroughly studied in [10]. Near threshold the final state interaction among the low energy electrons in the continuum and the fast Auger electron [11], named Post Collision Interaction (PCI), induces a shift and broadens the lineshape of the Auger peaks. PCI phenomenon in argon has been investigated by electron impact in [12–14], in $(e–2e)$ experiments by [15–18]. Cascade effects on the Ar LMM Auger spectrum have been investigated in [19] using both electron and X-ray beam as well with a broad-band synchrotron radiation in [20]. Theoretical calculations and comparison with experiments were done in [21–23] as well as in [20], where a relativistic configuration average approximation has been used.

In this work, we present the Auger electron spectra of argon in the kinetic energy region between 135 and 235 eV and compare them with previous studies by electron impact [7,8,12,13]. The aim is to present high-resolution electron spectra with a large number of new features, in some cases left unassigned, with the hope that the precise determination of their energy positions can trigger novel theoretical studies.

* Contribution to the Topical Issue "Low-Energy Positron and Positronium Physics and Electron-Molecule Collisions and Swarms (POSMOL 2019)", edited by Michael Brunger, David Cassidy, Saša Dujko, Dragana Maric, Joan Marler, James Sullivan, Juraj Fedor.

[a] e-mail: bratislav.marinkovic@ipb.ac.rs

The Auger spectra have been measured at several impact electron energies (243, 313, 323, 808, 909 and 2019 (±0.4) eV and ejection angles of 60°and 90°. The lowest incident electron energies have been chosen to cover the energy regions around the ionization of the $2p$ and $2s$ inner shells at (248–250) and 326 eV respectively. The aim was to disentangle the contribution to the spectra due to the opening of new channels as for example the ionization of the $2s$ inner shell. Then the energy of 323 eV, i.e. in the region of the $2s \rightarrow 4p$ excitation, was chosen to eventually identify the contribution of resonant Auger transitions. The energies 808, 909 eV are close to the maximum cross section for the Ar $2p$ ionization cross section. At the energy of 2019 eV no new channels are opened, because the ionization energy of the $1s$ inner shell is at about 3206 eV. The aim of this latter measurement was to present high resolution spectra at an energy close to the ones previously measured by Werme et al. [7]. The majority of the spectra has been obtained at 90° ejection angle, but due to the best signal to background ratio some measurements have been done the angle of 60°. This would not affect the comparison of the spectra at different energy, because the angular asymmetry of the Auger transitions is very small and for the purposes of this work the Auger emission can be considered isotropic. The experiments at low incident energy allow to investigate the influence of the PCI phenomenon on the line-shape and the energy position of the different features in the Auger spectrum between 200 and 209 eV.

The assignments of the observed features were not straightforward due to existence of difference between experiments and calculations, even among calculations for several features. For this reason all known assignments are presented in Table 1. All over the paper the relative intensity with respect to the intensity of the L_3-$M_{2,3}M_{2,3}(^1S_0)$ state is presented only for completely separated features.

The paper is organized as follows. Section 2 is devoted to some experimental details, while in Section 3 the full LMM Auger spectrum is split in six energy regions, which are separately discussed. Finally Section 4 is devoted to some conclusions.

2 Experiment

The experimental setup has been described in details elsewhere [1] and only some information relevant to this work are reported here. A non-monochromatic electron beam (10–2500 eV) collides with an atomic beam emitted from a platinum–iridium non-biased needle with internal diameter of 0.5 mm in the perpendicular direction to the scattering plane. The ejected electrons are analyzed by a high-resolution hemispherical analyzer with a mean radius of 125 mm and detected with seven channeltrons. The analyzer operates at a pass energy of 1 or 5 eV with defined retarding ratio and defined magnification determined by the two stage 11 element lens system. In these measurements all spectra are obtained in Constant Retarding Ratio (CRR) mode in which the ejected electrons are retarded by the lens stack by a constant proportion of their kinetic energy (KE). In that way the ratio of the KE to continuously varied pass energy during the scan was constant. This combination should provide uniform high transmission and acceptance angle of (±1°). The background pressure in the vacuum chamber was 6×10^{-8} mbar, while the working pressure with argon gas was 2×10^{-6} mbar. With an electron current of 10^{-6} A typical accumulation time for most of the spectra was 60 min with energy step of 0.020 or 0.050 eV per channel.

The energy resolution of the ejected electron spectra is determined by the energy resolution of the analyzer and Doppler broadening of 0.007 eV at temperature of 350 K and mean kinetic energy of 12 eV. The resolution of measured peaks defined as full width at half maximum (FWHM) varied from 0.050 to 0.080 eV in the region of low ejection energy. In the ejected electron spectrum both scattered and ejected electrons contribute to the continuum background, while the Auger transitions appear as well defined features. All spectra are presented with subtracted background without any further normalization of the obtained data. The subtraction is made using linear functions and does not affect the signal due to the discrete states.

For the calibration of Auger electron energy the line at 11.72 eV from the Ar $[3s3p^6 3d(^1D)]$ excited state (27.48 eV) was used. The energy of this line was obtained from an argon–helium mixture at 303 eV incident electron energy. The reference was the energy position of the double excited $2s2p(^1P)$ state in He at 60.130 eV (35.55 eV ejected energy) [24]. The quality of the energy calibration was checked on the $L_3M_{2,3}M_{2,3}(^1S_0)$ line in the Auger spectra. The position of this line was found to be at (200.960 ± 0.020) eV, i.e. 0.130 eV lower than the value obtained by Werme et al. [7] for the same line (201.09 eV). The scale of the incident energy between 30 and 200 eV has been calibrated using the elastic channel. For higher energies, the fit made between 30 and 200 eV was applied. The FWHM of the elastic peak was roughly 0.80 eV.

3 Results and discussion

The $L_{2,3}MM$ Auger transitions occur when the incident energy of the impact particles (X-ray, ion, UV-photon, electron) is higher than the binding energy of $L_{2,3}$ subshells which are 248.62 and 250.77 eV for L_3 and L_2 respectively [25] with a splitting of 2.15 eV between the two subshells. When a vacancy is formed in the L shell an outer electron fills the vacancy and the excess energy is used to eject another outer electron leading to an Ar^{2+} ion with two vacancies in the M shell. The $L_{2,3}MM$ Auger spectrum obtained at high resolution is composed of a wealth of features with different energy widths and intensities [7,10,13]. These features come not only from the direct ionization of the $L_{2,3}$ subshells, but also from transitions following the decay of $(2p^{-1}nl^{-1}n'l')$ excited singly ionized initial states or from doubly charged ionized states populated either by a shake-off in the primary ionization or Coster-Kronig transitions from $2s$ ionization [7].

Figure 1 shows three ejected electron spectra obtained at 324, 909 and 2019 eV in the kinetic energy region (135–159) eV. The spectrum at 324 ± 0.4 eV, at an

Table 1. Kinetic energies KE (eV) and labels of the features in argon Auger spectra obtained in the kinetic energy region (135–235) eV. The uncertainty in KE energy is ±0.020 eV.

This work label	KE (eV)	Relative intensity	[Ref.]: Line N^0, in reference assignment/transition
1	134.93		
2	136.87		
3	139.12		
4	139.74		
5	140.91		
6	141.35		
7	142.07		
8	145.13		
9	146.53	0.07	[7]: 1
10	147.45		
11	148.02		
12	148.72		[7]: 2
13	149.17		[7]: 3 [20]: $2p^5 3s^2 3p^4 \rightarrow 3s^0 3p^4(^1D_2)$, $n = 12$ (calc., exp.)
14	149.67		
15	150.23		
16	150.77		[7]: 4
17	151.55		[7]: 5
18	152.01		[7]: 6
19	153.15		[7]: 7
20	154.29		
21	155.73		
22	157.61		[7]: 8 (at 157.26 eV)
23	158.63		
24	159.44		
25	160.25		[7]: 9
26	160.57	0.15	[7]: 10 L_3-$[3s3p^2]3d$ [22]: $N_0 11$
27	161.21		
28	162.15		[7]: 11 L_3-$3s^2 3p^4 3d^2$ [10] L_3-$M_1 M_{2,3}(^1P)$ [21]: 11 L_3-$[3s3p^2]3d$ [22]: 11 $N_0 10$
29	162.69		[7]: 12 L_2-$[3s3p^2]3d$[22]: $N_0 11$,
30	163.83		$3p^3(^2D)8d(^3P)$
31	164.34		$3p^3(^2D)6d(^3P)$, $3p^3(^2D)7d(^3P)$ [7]: 13 L_2-$3s^2 3p^4 3d^2$ [10]: L_2-$M_1 M_{2,3}(^1P)$ [21]: 13 L_2-$[3]3p^2 3d$ [2]: $N_0 10$
32	164.71		[7]: 14
33	165.05		$3p^3(^2D)7s$ [7]: 15
34	166.05		$3p^3(^2D)8d(^3P)$ $3p^3(^2D)6d(^3F)$
35	166.57		$3p^3(^2P)5d(^3P)$ $3p^3(^2D)6d(^3P)$, $3p^3(^2D)7d(^3P)$
36	166.69		[7]: 16
37	166.97		
38	167.32		$3p^3(^2D)7s$ [7]: 17 [20]: $2p^5 3s^2 3p^4 \rightarrow 3s^1 3p^3(^1D_2)$, $n = 17$ (calc.), or [20]: $2p^5 3s^1 3p^5 \rightarrow 3s^0 3p^4(^1D_2)$, $n = 35$ (calc.)
39	167.79		$3p^3(^2D)6s(^{3,5}D)$, $3p^3(^2D)5d(^3P)$, [7]: 18

Table 1. Continued.

This work label	KE (eV)	Relative intensity	[Ref.]: Line N^0, in reference assignment/transition
40	168.04		$3p^3(^2D)6d(^3F)$
41	168.82		$3p^3(^2P)5d(^3P)$
			$3p^3(^4S)5d(^{3,5}S)$
42	169.17		[7]: 19
43	169.59		[20]: $2p^5 3s^2 3p^4 \rightarrow 3s^1 3p^3(^3D_3)$, $n = 17$ (calc.)
44	169.92		$3p^3(^2D)6s(^{3,5}D)$, $3p^3(^2D)5d(^3P)$,
45	171.01		$3p^3(^4S)5d(^{3,5}S)$,
			[10]: 21a
			[20]: $2p^5 3s^2 3p^4 \rightarrow 3s^1 3p^3(^3D_3)$, $n = 17$ (calc.)
46	171.49	0.06	L_3-$3s^2 3p^3(^2D)4d(^3P)$, [7]: 21; [10]: 2—b
			L_3-$M_1M_{2,3}(^1P)$ [21]: 21
			L_3-$3p^3](^2D^0)4d(^3P^0)$ [22]: N_0 8
47	173.45		$3p^3(^2P)4p(^1S_0)$
			L_3-$3s^2 3p^3(^2P)4p(^1S_0)$ [23], [10]: 22a
			[7]: 22
			L_3-$[3p^3](^2P^0)4p\,^1S$ [22]: $N_0$7
48	174.07		$3s^0 3p^6$
			L_3-$M_1M_1(^1S_0)$ [7,21]: 24
			L_3-$[3s^2]\ ^1S$ [22]: $N_0$6
49	174.81		[7]: 25
			[22]: L_3-$[3s^2]\ ^1S$ [18]
50	175.65		$3p^3(^2P)4p(^1S_0)$
			L_2-$3s^2 3p^3(^2P)4p(^1S_0)$ [23], [10]: 26a
			[7]: 26
			L_2-$M_1M_1(^1S)$ [21]: 26
			L_2-$[3p^3](^2P^0)4p\,^1S$ [22]: $N_0$7
51	176.23		$3s^0 3p^6$
			[7]: 29
			L_2-$M_1M_1(^1S)$ [21]: 29, [10]
			L_2-$[3s^2]\ ^1S$ [22]: $N_0$6
52	176.51		$3p^3(^2D)4p$
			[7]: 30
			L_2-$[3s^2]\ ^1S$ [22]
53	177.27		$3p^3(^2D)4p$
			[7]: 31
			[10]: 31b
			L_2-$3s^2 3p^3(^2P)4p(^3P_1)$ [23]
54	177.81	0.49	$3p^3(^2P)3d$
			L_3-$M_1M_1(^1S_0)$ [7]: 32,
			[10] :32a
			L_2-$M_1M_1(^1S)$ [21]: 32
			L_3-$M_1M_{2,3}(^1P)$ [21]: 32
			L_3-$[3p^3](^2P^0)3d\ ^1P^0$[22]: $N_0$5
55	178.53		$3p^3(^2P)3d\ (^3P_{2,1,0})$
			L_3-$3s^2 3p^3(^2P)3d(^3P)$ [7]: 34
			L_2-$3s^2 3p^3(^2D)4p(^3P_1)$ [23]
			[10]: 34
			L_3-$M_1M_{2,3}(^1P)$ [21]: 34
			[20]: $2p^5 3s^2 3p^4 \rightarrow 3s^2 3p^2(^1S_0)$, $n = 12$ (calc., exp.)
56	178.87		$3p^3(^2D)4p$
			$3p^3(^4S)3d\ (^3P_{2,1,0})$
			L_3-$3s^2 3p^3(^2P)4s(^1P)$ [7]: 35
			L_3-$[3p^3](^2P^0)4s\ ^1P^0$[22]: $N_0$2
			$L_3M_1M_{2,3}(^1P)$ [21]: 35
57	179.37		$3p^3(^2D)4p$
			L_3-$3s^2 3p^3(^2P)4s(^3P)$ [7]: 36
			[10]: 36

Table 1. Continued.

This work label	KE (eV)	Relative intensity	[Ref.]: Line N^0, in reference assignment/transition
			L_3-$M_1M_{2,3}(^3P)$ [21]: 36
			L_2-$[3p^3](^2P^0)4s^3P^0$[22]: $N_0$5
			L_2-$3s^23p^3(^2D)4p(^1P_1)$ [23]
58	179.95	0.23	$3p^3(^2P)3d$
			L_2-$M_1M_1(^1S_0)$ [7]: 37
			[10]: 37a
			L_2-$M_1M_{2,3}(^1P)$ [21]: 37
			L_3-$[3p^3](^2D^0)3d^1P^0$[22]: $N_0$4
59	180.61		$3p^3(^2P)3d$ $(^3P_{2,1,0})$
			L_2-$3s^23p^3(^2P)3d(^3P)$ [7]
			[10]: 38
			L_2-$M_1M_{2,3}(^1P,^3P)$ [21]: 38 or 39
			L_2-$[3p^3](^2D^0)3d^3P^0$[22]: $N_0$3
60	181.08		$3p^3(^4S)3d$ $(^3P_{2,1,0})$
			L_2-$3s^23p^3(^2P)4s(^1P)$ [7]: 40
			[10]: 40
			$L_2M_1M_{2,3}(^1P)$ [21]: 40
			L_2-$[3p^3](^2P^0)4s^1P^0$[22]: $N_0$2
			[20]: $2p^53s^23p^4 \rightarrow 3s^23p^2(^1D_2)$, $n = 12$ (calc., exp.)
61	181.97		[7]: 42
			L_2-$3s^23p^3(^4S)4p(^5P_2)$ [23]
			[20]: $2p^53s^23p^4 \rightarrow 3s^23p^2(^1S_0)$, $n = 18$ (calc., exp.)
62	182.93		[20]: $2p^53s^23p^4 \rightarrow 3s^23p^2(^3P_2)$, $n = 13$ (calc.)
63	187.23	0.67	L_3-$M_1M_{2,3}(^1P_1)$ [7,10]: 45
			L_3-$M_1M_{2,3}(^1P)$ [21]:
			L_3 -$(^1P_1)$ [6,19,26]
64	188.49		[7]: 47
			[20]: $2p^53s^23p^4 \rightarrow 3s^23p^2(^3P_1)$, $n = 21$ (calc.)
65	189.37	0.36	L_2-$M_1M_{2,3}(^1P_1)$ [7,10]: 48
			L_2-$M_1M_{2,3}(^1P)$ [21]: 48
			L_2 -$(^1P_1)$ [6,19,26]
66	189.99		$L_{2,3}$-$M_{2,3}(^1P_1)$-$M^3{}_{2,3}(^2P)$ [7]: 49
67	190.27		$L_{2,3}$-$M_{2,3}(^3D_3)$-$M^3{}_{2,3}(^2P)$ [7]: 50
68	190.55		[7]: 51
			L_3 -$(^3P_0)$ [26]
69	190.97		L_3-$M_1M_{2,3}(^3P_2)$ [7,10]: 52, 52b
			L_3-$M_1M_{2,3}(^3P)$ [21]: 52
			L_3 -$(^3P_2)$ [6,19,26]
70	191.45		$L_{2,3}$-$M_{2,3}(^3D_2)$-$M^3{}_{2,3}(^2P)$ [7]: 54
71	191.73		$L_{2,3}$-$M_{2,3}(^1P_1)$-$M^3{}_{2,3}(^2D)$ [7]: 55
72	191.99		$L_{2,3}$-$M_{2,3}(^3D_3)$-$M^3{}_{2,3}(^2D)$ [7]: 56
73	192.57		$L_{2,3}$-$M_{2,3}(^3D_1)$-$M^3{}_{2,3}(^2P)$ [7]: 58
			[19]: Peak I
74	192.95		L_2-$M_1M_{2,3}(^3P_0)$ [7]: 59, 60a
			L_2-$M_1M_{2,3}(^3P)$ [21]: 59
			L_2 -$(^3P_0)$ [6,26]
75	193.17		L_2,-$M_1M_{2,3}(^3P_1)$ [7,10]: 60, 60b
			L_2 -$(^3P_0)$ [26]
			[19]: Peak H
76	193.87		[7]: 62
77	194.33		$L_{2,3}$-$M_{2,3}(^3D_1)$-$M^3{}_{2,3}(^2D)$ [7]: 63
78	194.51		$L_{2,3}$-$M_{2,3}(^1D_2)$-$M^3{}_{2,3}(^2P$[7]: 64
			[19]: Peak G
79	195.45		[7]: 65
80	195.81		[7]: 66
81	196.25		$L_{2,3}$-$M_{2,3}(^1D_2)$-$M^3{}_{2,3}(^2D)$ [7]: 67
82	196.45		[19]: Peak F
83	197.89		[7]: 69
			[19]: Peak E

Table 1. Continued.

This work label	KE (eV)	Relative intensity	[Ref.]: Line N^0, in reference assignment/transition
84	200.96	1.00	L_3-$M_{2,3}M_{2,3}(^1S_0)$ [7,10,13,21]: 72 [19]: Peak D
85	203.09		L_2-$M_{2,3}M_{2,3}(^1S_0)$ [7,10,13,21]: 73
86	203.35	4.09	L_3-$M_{2,3}M_{2,3}(^1D_2)$ [7,10,13,21]: 74 [19]: Peak C
87	205.09	3.23	L_3-$M_{2,3}M_{2,3}(^3P_{0,1,2})$ [7,10,13,21]: 75, 75 a,b,c [19]: Peak B
88	205.51	2.40	L_2-$M_{2,3}M_{2,3}(^1D_2)$ [7,10,13,21]: 76
89	207.11	1.39	L_2-$M_{2,3}M_{2,3}(^3P_{0,1,2})$ [7,10,13,21]: 78, 78 a,b,c [19]: Peak A
90	207.87		
91	208.39		[20]: $2p^4(^1S_0) \rightarrow 2p^5 3s^1 3p^5$, $n = 39$ (calc.)
92	208.71		
93	209.97		[7]: 80
94	211.65		[7]: 81
95	213.15		[7]: 82
96	215.41		
97	219.37		[20]: $2p^4(^1D_2) \rightarrow 2p^5 3s^2 3p^4$, $n = 13$ (calc.)
98	222.49		[20]: $2p^4(^1D_2) \rightarrow 2p^5 3s^2 3p^4$, $n = 2$ (calc.)
99	224.37		[20]: $2p^4(^1S_0) \rightarrow 2p^5 3s^2 3p^4$, $n = 20$ (calc.)
100	225.59		[20]: $2p^4(^1S_0) \rightarrow 2p^5 3s^2 3p^4$, $n = 18$ (calc., exp.)
101	227.25		[20]: $2p^4(^1S_0) \rightarrow 2p^5 3s^2 3p^4$, $n = 15$ (calc.)
102	227.97		
103	229.53		[20]: $2p^4(^1S_0) \rightarrow 2p^5 3s^2 3p^4$, $n = 12$ (calc.)
104	231.17		

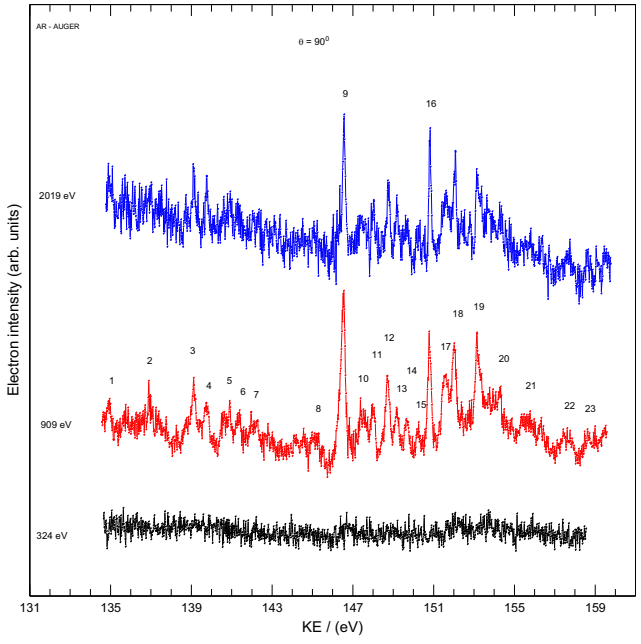

Fig. 1. The Auger electron spectra in the kinetic energy region (135–159) eV measured at 90° of ejection angle at incident electron energies (324, 909 and 2019 eV). The spectra are shown with subtracted background without normalization of data. The energy step is 0.020 eV.

incident energy above the $2p(L_{2,3})$ ionization thresholds, but below the $2s(L_1)$ shell ones, does display no features, indicating that in this region there is no direct contribution from the Auger electrons produced from the decay of the $2p$ holes. At higher incident energies (909 and 2019 eV) the figure shows 23 features distributed over two energy regions (135–146) and (146–159) eV. The energies of these features are listed in Table 1.

In the first energy region the features (1–7) are observed with low intensities and not well defined shape in the spectrum at 909 eV incident energy, while the poor statistics of the one at 2019 eV allows a clear observation of features 3–4 and, maybe, 5–7. To our best knowledge in previous investigations of the $L_{2,3}MM$ electron spectra this region was not directly studied. However, in a recent multi-electron spectroscopy investigation of the decay of the $2s$ hole by Lablanquie et al. [26] the cascade process leading to the triply and quadruple ionized Ar atom has been investigated. In the cascade leading to Ar^{4+} ion these authors identify in the energy distribution of the last two Auger electrons ejected from the decay of the intermediate Ar^{2+} $2p^{-1}3p^{-1}$ or $2p^{-1}3s^{-1}$ states a broad unresolved contribution between 120 and 140 eV in the case of the decay from the $2p^{-1}3p^{-1}$ intermediate states and between 130 and 150 eV for the other states. Thus is not unreasonable to assume that the features 1–7 can correspond to a decay to triply ionized states located above the first Ar^{4+} states, whose binding energy is located by [26] between 140 and 160 eV, which then autoionize emitting a low energy electron to Ar^{4+} continuum.

The second energy region (146–159) eV shows features with higher intensities and better defined line shapes. This energy region was studied by electron impact in [7] and six

features have been identified with no assignment. In [20] a broad band X-ray radiation has been used to ionize the K-shell of Ar and the cascade processes from the $L_{23}L_{23}$ and $L_{23}M_{23}$ double core holes has been investigated both experimentally and theoretically. In the spectrum in Figure 6 of [20] an intense feature at about 149.1 eV and a few other minor features in the region of our structures (10–21) are observed, while the broad feature on rising background towards 160 eV in Figure 6 of [20] does not find a correspondence in our spectrum. The Dirac-Fock calculations of [20] allow to assign to the $L_{23}M_{23}^2$-$M_1^2M_{23}^2$ ($2p^53s^23p^4 \rightarrow 3s^03p^4$) transitions in the region below 155 eV. In our spectrum the most intense feature (9) at 146.53 eV has a FWHM of about 0.26 eV and a relative intensity to feature (84) in Figure 5, corresponding to the L_3–$M_{23}M_{23}(^1S_0)$ transition, of 0.07 at 909 eV incident energy spectrum. This feature does not appear to be observed in [20], while its position well compares with feature (1) in [7], although in [7] its relative intensity to the L_3–$M_{23}M_{23}(^1S_0)$ transition is only 0.02. Another possible contribution to the features in this region can come from the cascade decay of the $2s$ initial hole to triply charged ion, as shown in the multi-coincidence experiment by Lablanquie et al. [26]. In their Figure 4 it is shown that the L_1-$L_{23}M_{23}$ Coster-Kronig Auger electrons (40–50 eV) are detected in coincidence with the faster electron of the electron pair produced in the decay to Ar^{3+} ion with kinetic energies in the range 150–160 eV. The possible contribution of the decay to Ar^{3+} can be inferred by the fact that we observe several pairs, e.g. (9,11), (10,13), (11,14), (12,15) and (13,16), with separation between 1.5 and 1.8 eV consistent with the energy splitting of the Ar^{3+} ^2P and ^2D states.

In Figure 2 the spectra in the kinetic energy region (159–173) eV obtained at 313, 324, 909 and 2019 eV incident energies are shown and the energies of the different observed features are listed in Table 1. The incident energies 313 and 324 eV are below the ionization of the $2s$ state. Both spectra are composed by broad features likely due to the PCI effect, that shifting and broadening the peaks observed at the higher incident energies make them overlapping at the lowest ones. In the spectra at 909 and 2019 eV about 22 narrow features can be distinguished. In the same region Werme et al. [7] identified 12 features, although with different relative intensity. For example the intensity ratio between features (26) and the L_3–$M_{2,3}M_{2,3}(^1S_0)$ line (84) in Figure 5 is 0.15, while the corresponding ratio in [7] is 0.05. Also Figure 6 of [20] shows a spectrum in this region with a similar shape, but with broad and unresolved features.

The first narrow feature (26) at 160.57 eV with FWHM of 0.10 eV at high incident energy is the most intense feature in this region separated by 0.32 eV from feature (25). At incident energy 323 eV we investigated the influence of the resolution of the apparatus to the line width of the feature (26) by comparing its FWHM with the one of the peak $3d(^1D)$ at 11.72 eV obtained under the same experimental conditions. It was found that when the width of $3d(^1D)$ peak is 0.090 eV, feature (26) has a width of 0.80 eV, while improving the resolution, to 0.050 eV for the $3d(^1D)$ peak, the width of feature (26) became 0.32 eV. This confirms, that the shape of the spectra at 313 and 323 eV is not due to a bad resolution of the set-up, but results from the overlap of a large number of lines broadened and shifted by the PCI effect. However, both spectra clearly show six defined structures, which indicate that in this region a large contribution come from the decay of the ionizing events involving $2p$ shells. This is further confirmed, by the fact that at higher incident energy several pairs of features, (26,29), (28,31), (30,34), (31,35), (33,38), (34,40), (35,41), (39,44) and (41,45), with energy separation close to 2.15 eV, the energy splitting between the $2p_{3/2,1/2}$ subshells, can be identified. Thus, these features can be assigned to a transition from the $2p^{-1}$ states to the Ar^{2+} satellite states. Previous assignment of these features relied on theoretical calculations by McGuire [21] and Dyall and Larkins [22]. They proposed an assignment for the first pair of features (26,29), which corresponds to lines (10,12) in [22], as $L_{2,3}$-$[3s3p^2]3d$ and for the second pair (28,31) with energies corresponding to their lines (11,13) as $L_{3,2}$-$M_1M_{2,3}(^1P)$ [21] and $L_{2,3}$-$[3s3p^2]3d$ [22]. The other pairs of features were not assigned. The high resolution threshold-photoelectron spectroscopy experiments by Avaldi et al. [27] which provided detailed information on the Ar^{2+} satellite states, can be used to propose an assignment for these features.

The spectrum in this region can also receive contributions from other decays channel as proposed in [20], where the spectrum due to the transition assigned as $L_{2,3}[M^2]$-$MM[M^2]$ has been calculated. Several calculated $2p^53s^23p^4 \rightarrow 3s^13p^3$ lines find a very good match (see Tab. 1) with some of the features observed in our spectrum. The relative importance of the decay of the $2p$ holes to the Ar^{2+} satellites or the cascade decay to Ar^{4+} following the $2s$ ionization, which may lead to a definite assignment of the different features, cannot be established without knowing the Ar $2p$ and $2s$ relative ionization cross section for electron impact at the different energies of the present measurements.

In Figure 3 the kinetic energy region 173–184.5 eV measured at the four incident energies is shown and the kinetic energies of the observed features are listed in Table 1. Apart from the narrowing of the peak due to reduction of the final state PCI effect on the line shape as the incident energy increases, all the main features are present already at the lower incident energy. This indicates that the main contribution to this region of the spectrum is due to ionization of the $L_{2,3}$ subshells. The spectrum at 323 eV is obtained at 60° in order to better resolve the structures due to a minor contribution of the background. At the lowest incident energy the asymmetric and broad line shapes show also a shift, which is in average about +0.080 eV at 323 eV. The most intense features (54 and 58) at 177.81 eV and 179.95 eV, respectively, with FWHM of 0.18 eV and an energy separation of 2.14 eV are assigned consistently with the previous literature to the $L_{3,2}$-M_1M_1 ($^1S_0$) transitions. The intensity ratios between features (54 and 58) and line (84) at 909 eV incident energy are 0.49 and 0.23, respectively, larger than the values 0.34 and 0.18 of the corresponding lines 32/72 in [7].

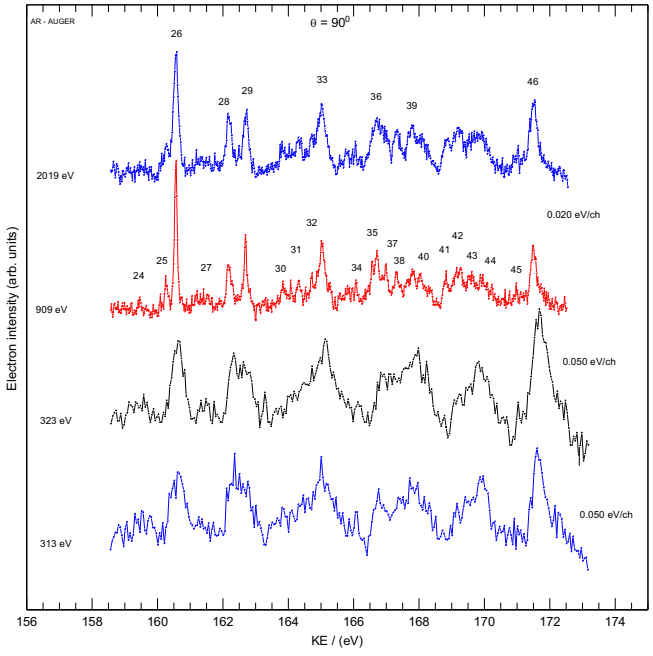

Fig. 2. As Figure 1, but for the kinetic energy region (159–173) eV.

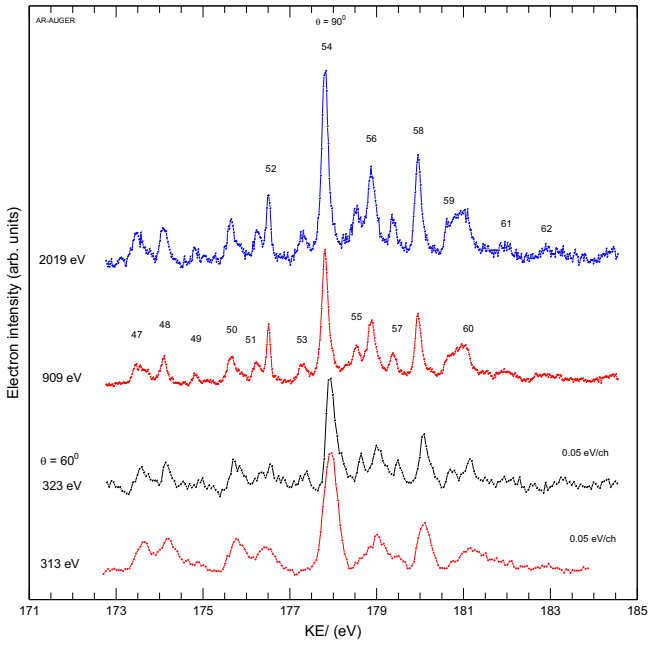

Fig. 3. As Figure 2, but for the kinetic energy region (173–184.5) eV. The spectrum at 323 eV was obtained at an ejection angle of 60° due to the better signal to background ratio.

In this energy region seven pairs of peaks (47,50), (48,51), (52,56), (53,57), (54,58), (55, 59) and (56,60), with an energy separation close to the splitting between the $2p$ subshells are clearly observed. The energies of the features (48,51) at 174.07 and 176.23 eV, respectively, are in very good agreement with the ones observed by Víkor et al. [13] (Fig. 1c) in their high resolution (68 ± 4 meV) study of the Auger $L_{2,3}MM$ lines by a 2 keV electron beam. The observation of these pairs indicates that the main process leading to the formation of these features is a decay of the Ar^+ $2p$ hole to an Ar^{2+} excited states. Thus, the process is a shake-up in the final state following Auger decay. These states have been characterized by threshold photoelectron–photoelectron coincidence experiment (TPEsCO) in [27]. The large numbers of states observed in that work is of course not observed in the Auger spectrum, but for the six pairs: (47,50), (48,51), (52,56), (53,57), (54,58), (55,59) and (56,60) we can propose the assignments for the Ar^{2+} finals states presented in Table 1.

Other possible transitions can populate this region. For example, the cascade following the $2s$ ionization and leading to the formation of the Ar^{3+} states with the Auger transitions $L_{2,3}$ M_{23}-M_1M_{23} M_{23}. These transitions can form pair of features separated by 1.7 eV, the energy separation of the Ar^{3+} ^2P and ^2D states. An example can be represented by lines (49,52). The feature (52) is the second narrow not completely resolved feature with FWHM of 0.1 eV which is 0.28 eV apart from the feature (51).

It is interesting to compare the influence of the PCI effect to the line broadening in experiments induced by photons [10] and electrons near threshold at 265 and 323 eV, respectively. In both experiments the resolution was similar, but the spectra in Figures 2 and 3 of [10] show higher intensities and smaller broadening than in the present experiment indicating stronger PCI effect in electron collision. This is because in electron impact close to the threshold the PCI effects are ruled by two low energy electrons, the ejected and scattered ones, while in photoionization PCI depends only on the interaction between the Auger electron and the photoelectron.

In Figure 4 four spectra in the energy region (186–199) eV at incident electron energies of 313, 323, 909 and 2019 eV are shown. The kinetic energies of the observed features are listed in Table 1. The spectra at 313 and 323 eV show only four intense features (63, 65, 69, 74) with energy separation close to 2.15 eV, the separation between the $2p_{3/2}$ and $2p_{1/2}$ states, with a broad asymmetric line shape (FWHM of 0.25 and 0.28 eV for the peaks 63 and 65 at 323 eV) and a shift of about +0.080 eV with respect the same lines at higher incident energy. Both the asymmetric line shape and the shift are attributed to the PCI effect. The fact that these features are the only one present below the $2s$ ionization threshold and their energy separation clearly make them assignable as $L_{23}M_1M_{23}(^1P, ^3P)$ lines as done in previous works [7,13]. A high-resolution spectrum of this region has been reported also in [13] (Fig. 1b), but the comparison with the present spectrum at 2 keV, reveals a slightly better resolution in our experiment.

The intensity ratios of the features 63, 65, 69 to the feature (84) in Figure 5 are 0.67, 0.36, 0.72 larger than the ones (0.53, 0.32, 0.87) of the corresponding lines in [7]. As for the other features in the spectrum, which appear at higher incident energy, we observe five pairs of features (66,71), (67,72), (70,75), (73,77) and (78,81), respectively. Their separation corresponds to the separation between the Ar^{3+} (^2P) and (^2D) states. Thus, they can be assigned to a cascade following $2s$ ionization and corresponds to the $L_{23}M_{23} - M_{23}^3$ transitions as proposed already by [7]

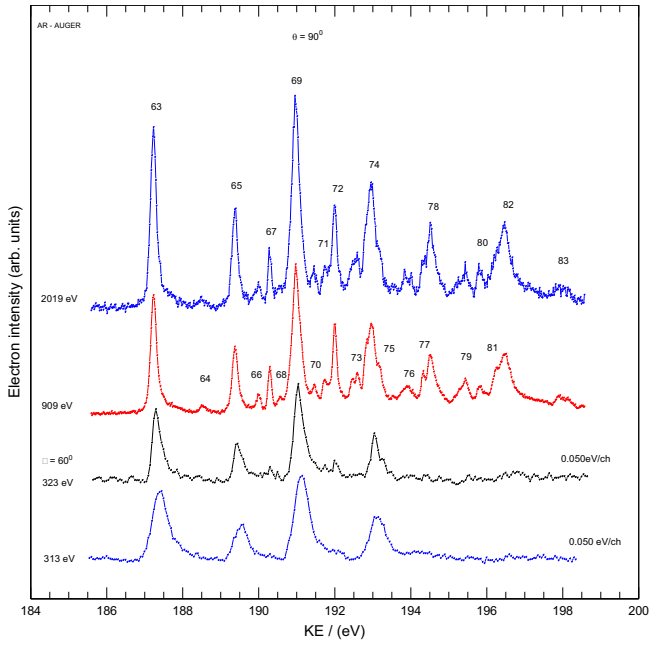

Fig. 4. As for Figure 3 but for the kinetic energy region (186–199) eV.

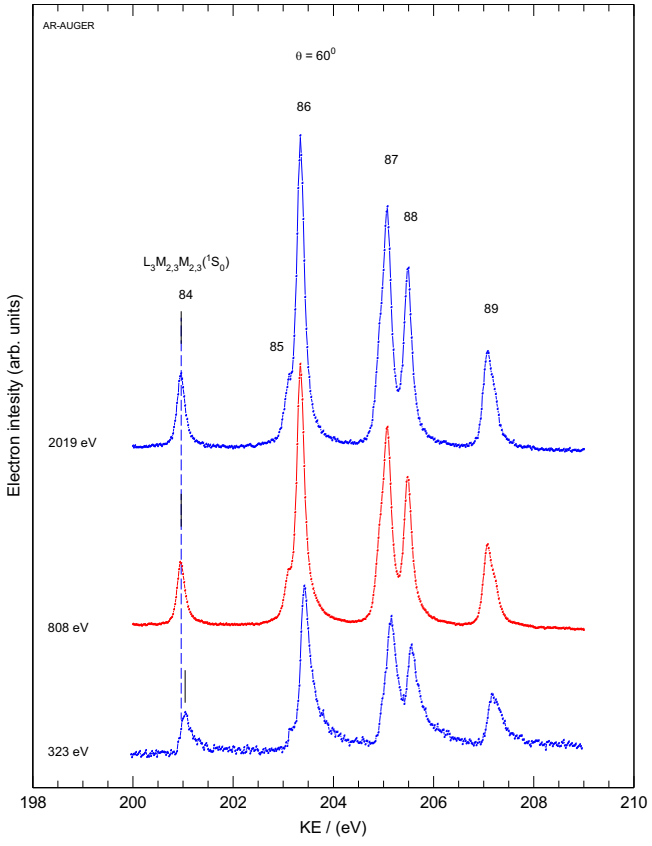

Fig. 5. As Figure 4 but for the kinetic energy region (199–209) eV.

and more recently proved by the multi coincidence experiments [26].

In this region it is interesting to note that the tiny feature (64), unassigned in previous Auger work [7], has been assigned in the study of the cascade Auger to a decay to Ar^{4+} with the final step assigned to the $2p^5 3s^2 3p^4 \rightarrow 3p^3(^3P)$ transition. Similar conclusion can be drawn by the multi-coincidence experiments by Lablanquie et al. [26] following Ar 2*s* ionization. The results from this latter work can be also invoked to explain the three features (76, 79 and 80) unassigned in previous work. They fall in region 193.5–196 eV which corresponds to the large feature in the Ar^{3+} binding energy spectrum populated in the cascade following Ar 2*s* ionization in [26].

Figure 5 shows three Auger spectra in kinetic energy region (199–209) eV measured at 323, 808 and 2019 eV. This is the region of the Auger $L_{2,3}$-$M_{2,3}M_{2,3}$ transitions, i.e. the direct decay of the 2*p* hole to the Ar^{2+} $3p^4$ (^3P,^1D and ^1S) states. This energy region was previously studied in several works [5–10,12,13,15–17]. The energy of all transitions and their assignments are listed in Table 1. Excellent agreement in the energy positions of the different features in this energy region between the present work and [13] was found, while some discrepancies with [7,10] are observed. The intensity ratios between the features in this energy region are: 4.09 for (86/84); 3.23 for (87/84); 2.40 for (88/84) and 1.34 for (89/84). The values determined in [7] for the ratio of the corresponding lines were: 2.70; 2.72; 1.83 and 1.39, respectively.

Indeed, the present spectra are obtained with a better resolution then the ones in [7,13]. The comparison of resolution between Werme et al. [7] and this work can be seen by comparing the line shapes of the feature (85) and the line 73 in spectra [7]. In both experiments the feature is observed as a shoulder not separated from the nearby feature, but it is slightly better resolved in the present work, as shown in Figure 5. In the case of [8] the resolution is comparable and those authors via a multiple peak fitting resolved the spin orbit components of the L_2-$M_{2,3}M_{2,3}$ and L_3-$M_{2,3}M_{2,3}$ ($^3P_{0,1,2}$) features. Even at our best experimental resolution of 0.045 eV, the FWHM is 0.180 eV and 0.170 eV, for the features (84) and (86) at high energies, due to the natural width of the Auger lines. At 323 eV incident energy the features show an asymmetric line shape and the FWHM of the (84) and (86) lines increases from the 0.17 eV/0.18 eV at 2019 eV incident energy to 0.25 eV/0.26 eV, respectively. Moreover, an energy shift of about 0.080 eV is observed. All these observations indicate that the spectrum at 323 eV incident energy is affected by the PCI.

In order to investigate the PCI effect on the shape and energy position of the features we measured the Auger spectrum in this region as a function of the impact electron energy down to 250 eV, i.e. near the ionization energy of the 2*p* state. In Figure 6 six spectra at incident electron energies from 244.10 eV to 323 eV are shown. Unfortunately, the experimental set-up did allow to resolve from the background all the L_{23}-$M_{2,3}M_{2,3}$ Auger lines only down to 262.30 eV incident energy (i.e. at 12.30 eV above the 2*p* threshold). At the lowest incident energies the most intense Auger features are barely visible above an oscillating background which makes any line shape analysis impossible. Studies of the influence of the PCI

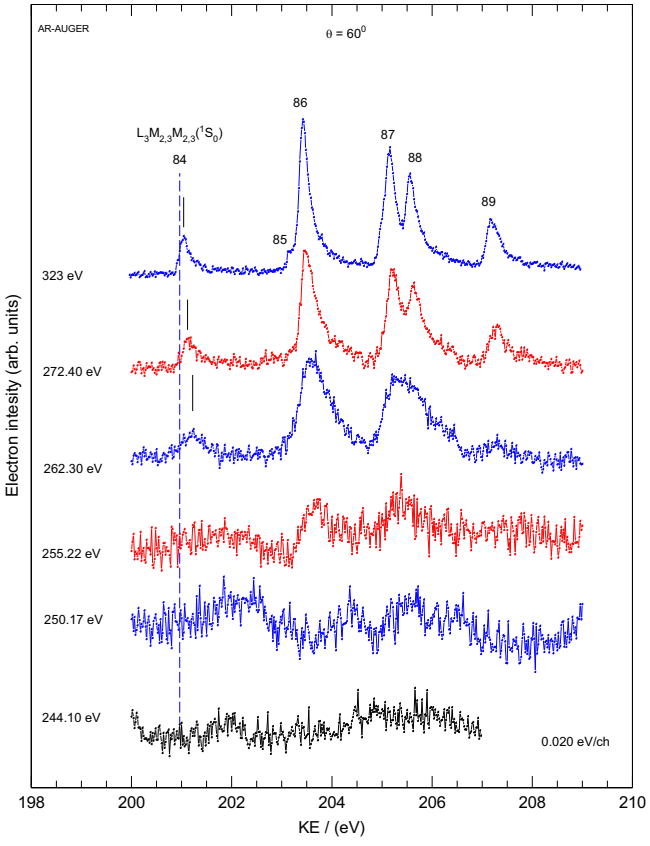

Fig. 6. The $L_{2,3}$-$M_{2,3}M_{2,3}$Auger kinetic energy region (200–209) eV at impact energies from 244.1 to 323 eV measured at 60° ejection angle with an energy step of 0.020 eV.

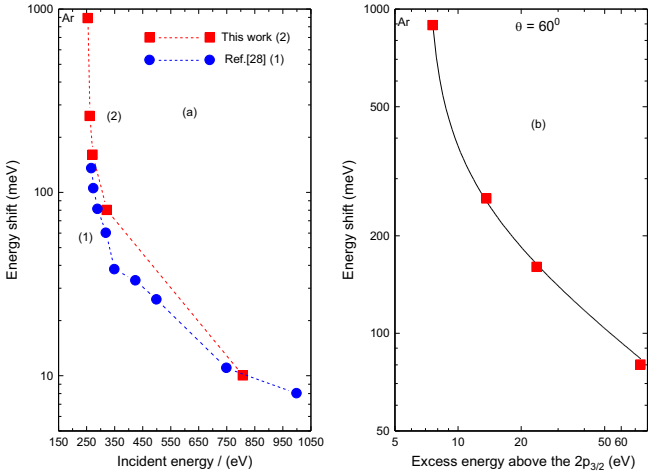

Fig. 7. (a, b) Energy shift of the $L_3M_{2,3}M_{2,3}(^1S_0)$ state. (a) Energy shift versus incident energy: (1) calculated values by Sheinerman et al. [28]; (2) present work. (b). Energy shift in log–log plot versus the excess energy above the ionization energy of the $2p_{3/2}$ (248.62 eV). The best fit gives the value of the power exponent (-0.48 ± 0.04).

effect on these Auger transitions have been reported also in [10,12,13].

To establish the energy shift of the feature due to PCI effect it is important to make a precise calibration of the electron impact energy and kinetic energy scale. The first was calibrated through the elastic channel as explained in Section 2. The calibration of the kinetic energy was more complicated. All spectra were measured in the same experimental conditions of pressure, pass energy in analyzer and lens parameters set in the CRR mode. The procedure included the verification of the energy position of the state $3d(^1D)$ at 11.72 eV as a benchmark two times, before and after measurements at each incident energy from 244 to 323 eV. Following this procedure, it was determined the effect of the PCI on the line shape and energy shift of the features. At 323 eV (Figs. 5 and 6) the shift is 80 meV in comparison with the position at incident energy of 2019 eV (Fig. 5), at 272.40 eV (160 meV), at 262.30 (260 meV), at 255.22 eV (890 meV) (Fig. 6) and at 808 eV (10 meV) (Fig. 5) as shown in Figure 7a. In the same figure we present a comparison of the energy shift (meV) of the first $L_3M_{2,3}M_{2,3}(^1S_0)$ transition measured here with an uncertainty of ±20 meV with the calculation of Sheinerman et al. [28] as a function of the incident energy. The shifts measured in our spectra at four different energies (from Figs. 5 and 6) are consistent with the calculation, although the theory appears to underestimate the measured shift as the ionization threshold is approached.

In order to investigate the energy shift of the $L_3M_{2,3}M_{2,3}(^1S_0)$ state as a function of the excess energy above the ionization energy (IP) of the $2p_{3/2}$ (248.62 eV), the shift is shown in log–log plot in Figure 7b. The functional dependence between shift and excess energy may be presented in the form $\Delta E_{\rm sh} = f(\Delta E_{\rm dif})^{\beta}$, where $(\Delta E_{\rm dif})^{\beta} = [E_0\text{–IP}(2p_{3/2})]^{\beta}$; $\Delta E_{\rm sh}$ is the shift of the position of the $L_3M_{2,3}M_{2,3}(^1S_0)$ (meV) at an incident energy E_0 with respect to the one at 2019 eV (Fig. 5) and the exponent β the fitting parameter. The best fit of the measured points gives the value of $\beta = (-0.48 \pm 0.04)$. This is close to the (-0.5) value obtained empirically by Barker and Berry [29] and Hicks et al. [30] for PCI effect in the case of autoionizing states of helium excited by rare gas ions and electrons, respectively.

Figure 8 shows high resolution spectra in the kinetic energy region 208–235 eV at 324, 909 and 2019 eV incident energies. There is a large difference between this region and the previous ones as for the number of the features and their intensities. The spectra shown in Figure 8 are the sum of several separate scans taken under the same experimental conditions with very long accumulation times and the background subtracted without normalization of obtained data. The energy of the feature (84) at 200.96 eV was used for the energy calibration of the spectra. At 909 eV three groups of features are visible, spanning from 208 to 213 eV, 214 to 224 eV and 224 to 233 eV. The spectrum at 324 eV incident energy shows no features above 212 eV indicating that the features (96–104) do not find their origin from the ionization of the $2p$ subshells. These features emerge in the spectra at higher incident energies indicating that their origin is from the C–K transitions following $2s$ ionization which produce only satellites.

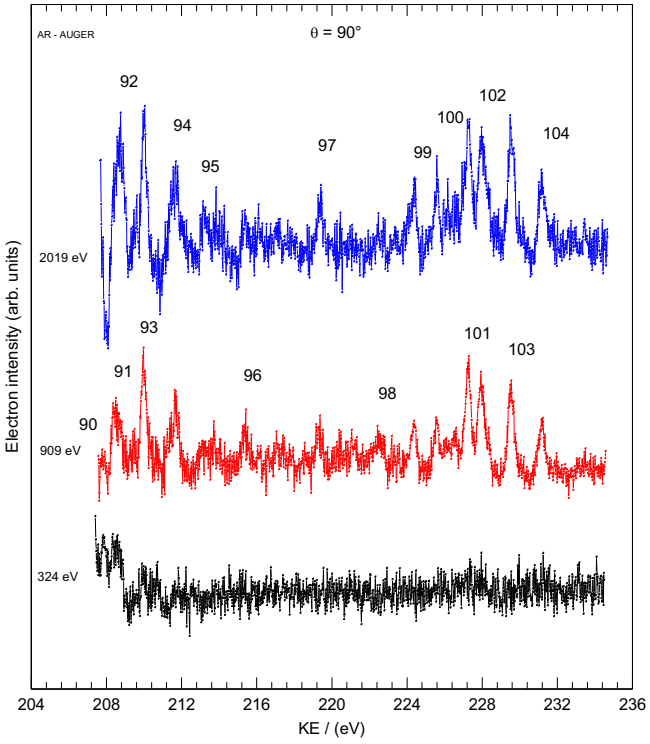

Fig. 8. As for Figure 6, but for the kinetic energy region (208–235) eV.

Hiltunen et al. [5] compared an $L_{2,3}$-$M_{2,3}M_{2,3}$ Auger spectrum by electron impact and the resonant Auger spectra obtained by synchrotron radiation at few energies corresponding to $2pns$, nd excitations. It is known that Resonant Auger lines occur at higher energy with respect to the $L_{2,3}$-$M_{2,3}M_{2,3}$ Auger lines and because the normal Auger contribution is much stronger than the structure due to resonant excitations in [5] a subtraction procedure had to be applied to prove the existence of some resonance lines in the electron impact spectrum. The features (90–94) in the present spectrum well fit with ones labelled C–G by [5]. However, the large number of transitions listed in Table 2 of [5] prevent a definite assignment. Moreover, the overlapping of a few features may explain the width of the features (0.3 eV). It is likely that also the features A and B of [5] are present in our spectra shown in Figure 5, but the large intensity of the normal Auger hampers their observation. The comparison can be made between feature (91) at 208.39 eV with energy position of calculated energy of the transition $2p^4(^1S_0) \rightarrow 2p^5 3s^1 3p^5$, labelled 9 in Table 3 of [20].

The next two energy regions from 214 to 233 eV were not studied systematically by electron impact or photoionization. Some information without assignments has been given in a study of Ar ionization by 20 keV proton beam (see Fig. 4 in [3]) with an energy resolution of 1.5 eV. Useful information was found in [20] from both theory and experiment. In that work a broad band synchrotron radiation is used to ionize mostly the K shell and partially the L_1 and $L_{2,3}$ shells. The energy position of the features labelled from (99) to (102) and reported in Table 1 shows very good agreement with calculated transitions in Table 3 of [20], but not with the experimental values reported in the same work. It is likely that the predominant ionization of the K shell obscures the low intensity features produced by the ionization of the L_1 shell.

Another possibility for the assignment of the features in this region is to consider the cascade decay of the $(2s^{-1})$ Ar^+ ion to the triply charged ion as discussed in the multicoincidence experiment by Lablanquie et al. [26]. In the coincidence map of Figure 4 in [26] these authors show the connection between the L_1-$L_{23}M$ Coster Kronig transitions and the $L_{23}M$-MMM decay leading to two structures between 210 and 230 eV. An assignment to this decay is supported by the fact that the pairs of features (100, 101) and (103,104), are separated by 1.66 and 1.64 eV, a value that, within the experimental uncertainty, matches the energy separation between of the ^2D and ^2P Ar^{3+} states.

4 Conclusions

Auger spectra in argon induced by electron impact have been studied systematically – in the kinetic energy regions 135–235 eV, at ejection angles of 60° and 90° degrees, for several incident electron energies from 243 to 2019 eV. The spectrum has been divided into six energy regions and every region was discussed in detail. The number of observed features is 104. The comparison of obtained results with previous works in [7,10,13] characterized by similar resolution, displays a reasonably good agreement in the energies of the features. However the higher resolution of the present work allowed us to observe a large number of satellite peaks in energy region 135 to 200 eV and new features in energy region 208 to 235 eV. For most of the features the assignment from previous works [7,10,20–23] was accepted, while some of the others have been assigned using the new information on the decay of the $Ar^+(2s^{-1})$ ion provided by multicoincidence experiments [26] and the ones on Ar^{2+} satellite states by threshold photoelectron-photoelectron coincidence experiments [26]. However a definite assignment of the full spectrum calls for new calculations.

In the region of $L_{2,3}$-$M_{2,3}M_{2,3}$ Auger transitions (200–209 eV) the strong influence of the PCI effect on the line shape, resolution and energy position of the features has been investigated at incident electron energies from 265 to 323 eV. It was found that the shift of the L_3-$M_{2,3}M_{2,3}(^1S_0)$ line in function of excess energy above the $2p$ ionization threshold has a dependency on the excess energy with the power exponent of (-0.48 ± 0.04), very close to the value of (-0.5) found in the case of the autoionizing decay of the doubly excited states of helium in [29] and [30].

The work has been performed under the project OI 171020 of MESTD of Republic of Serbia and the Italy-Serbia bilateral project particular relevance (Grande Rilevanza) “Nanoscale insights in radiation damage”. We acknowledge the partial support of COST Action CM1204 “XUV/X-ray light and fast ions for ultrafast chemistry (XLIC)”. One of us, J.J.J, is grateful to the Institute of Physics Belgrade for using their material

resources and to X. Urbain for his interest and support of this work.

Author contribution statement

Experimental data and drafting manuscript: J.J.J.; discussion and analysis of data, corrections and final version of the manuscript: J.J.J., B.P.M. and L.A.

References

1. J.J. Jureta, B.P. Marinković, L. Avaldi, Eur. Phys. J. D **70**, 199 (2016)
2. G. Johansson, J. Hedman, A. Berndtsson, M. Klasson, R. Nilsson, J. Electron Spectrosc. Relat. Phenom. **2**, 295 (1973)
3. G.N. Ogurtsov, I.P. Flaks, S.V. Avakyan, Sov. Phys. JETP **30**, 16 (1970)
4. M.E. Rudd, T. Jorgensen Jr., D.J. Volz, Phys. Rev. **151**, 28 (1966)
5. A. Hiltunen, T. Kylli, J. Mursu, O.P. Sairanen, H. Aksela, S. Aksela, J. Electron Spectrosc. Relat. Phenom. **87**, 203 (1998)
6. W. Mehlhorn, D. Stalherm, Z. Phys. **217**, 294 (1968)
7. L.O. Werme, T. Bergmark, K. Siegbahn, Phys. Scr. **8**, 149 (1973)
8. D. Ridder, J. Dieringer, N. Stolterfoht, J. Phys. B **9**, L307 (1976)
9. M. Žitnik, M. Kavčič, K. Bučar, B. Paripás, B. Palásthy, K. Tőkési, Nucl. Instrum. Methods Phys. Res. B **267**, 260 (2009)
10. H. Pulkkinen, S. Aksela, O.-P. Sairanen, A. Hiltunen, H. Aksela, J. Phys. B **29**, 3033 (1996)
11. M.Y. Kuchiev, S.A. Sheinerman, Sov. Phys. Tech. Phys. **32**, 879 (1987)
12. Y. Iketaki, T. Takayanagi, K. Wakiya, H. Suzuki, F. Koike, J. Phys. Soc. Jpn. **57**, 391 (1988)
13. G. Víkor, L. Tóth, S. Ricz, Á. Kövér, J. Végh, B. Sulik, J. Electron Spectrosc. Relat. Phenom. **83**, 235 (1997)
14. B. Paripás, G. Víkor, K. Tőkési, A. Hiltunen, Nucl. Instrum. Methods Phys. Res. B **154**, 209 (1999)
15. B. Paripás, B. Palásthy, Nucl. Instrum. Methods Phys. Res. B **267**, 275 (2009)
16. B. Paripás, B. Palásthy, M. Žitnik, K. Tőkési, Nucl. Instrum. Methods Phys. Res. B **279**, 66 (2012)
17. G. Stefani, L. Avaldi, A. Lahmam-Bennani, A. Duguet, J. Phys. B **19**, 3787 (1986)
18. D.K. Waterhouse, J.F. Williams, J. Phys. B **30**, 2845 (1997)
19. J.W. Cooper, S.H. Southworth, M.A. MacDonald, T. LeBrun, Phys. Rev. A **50**, 405 (1994)
20. F. von Busch, U. Kuetgens, J. Doppelfeld, S. Fritzsche, Phys. Rev. A **59**, 2030 (1999)
21. E.J. McGuire, Phys. Rev. A **11**, 1880 (1975)
22. K.G. Dyall, F.P. Larkins, J. Phys. B **15**, 2793 (1982)
23. J.E. Hansen, W. Persson, J. Phys. B **20**, 693 (1987)
24. R.P. Madden, K. Codling, Phys. Rev. Lett. **10**, 516 (1963)
25. G.C. King, M. Tronc, F.H. Read, R. Bradford, J. Phys. B **10**, 2479 (1977)
26. P. Lablanquie, S.M. Huttula, M. Huttula, L. Andric, J. Palaudoux, J.H.D. Eland, Y. Hikosaka, E. Shigemasa, K. Ito, F. Penent, Phys. Chem. Chem. Phys. **13**, 18355 (2011)
27. L. Avaldi, G. Dawber, N. Gulley, H. Rojas, G.C. King, R. Hall, M. Stuhec, M. Zitnik, J. Phys. B **30**, 5197 (1997)
28. S.A. Sheinerman, W. Kuhn, W. Mehlhorn, J. Phys. B **27**, 5681 (1994)
29. R.B. Barker, H.W. Berry, Phys. Rev. **151**, 14 (1966)
30. P.J. Hicks, S. Cvejanovic, J. Comer, F.H. Read, J.M. Sharp, Vacuum **24**, 573 (1974)